A Simple Tropical Atmosphere Model of Relevance to Short-Term Climate Variations*

BIN WANG AND TIANMING LI

Department of Meteorology, School of Ocean and Earth Science and Technology, University of Hawaii, Honolulu, Hawaii

(Manuscript received 5 November 1991, in final form 15 April 1992)

ABSTRACT

The tropical atmosphere model presented here is suitable for modeling both the annual cycle and short-term (monthly to decadal time scale) climate fluctuations in sole response to the thermal forcing from the underlying surface, especially the ocean surface. The present model consists of a well-mixed planetary boundary layer and a free troposphere represented by the gravest baroclinic mode. The model dynamics involves active interactions between the boundary-layer flow driven by the momentum forcing associated with sea surface temperature (SST) gradient and the free tropospheric flow stimulated by diabatic heating that is controlled by the thermal effects of SST. This process is demonstrated to be essential for modeling Pacific basinwide low-level circulations. The convective heating is parameterized by a SST-dependent conditional heating scheme based upon the proposition that the potential convective instability increases with SST in a nonlinear fashion.

The present model integrates the virtue of a Gill-type model with that of a Lindzen–Nigam model and is capable of reproducing both the shallow intertropical convergence zone (ITCZ) in the boundary layer and the deep South Pacific convergence zone (SPCZ) and monsoon troughs in the lower troposphere. The precipitation pattern and intensity, the trade winds and associated subtropical highs, and the near-equatorial trough can also be simulated reasonably well.

The thermal contrast between oceans and continents is shown to have a profound influence on the circulation near landmasses. Changes in land surface temperature, however, do not exert significant influence on remote oceanic regions. Both the ITCZ and SPCZ primarily originate from the inhomogeneity of ocean surface thermal conditions. The continents of South and North America contribute to the formation of these oceanic convergence zones through indirect boundary effects that support coastal upwelling changing the SST distribution. The diagnosis of observed surface wind and pressure fields indicates that the nonlinear advection of momentum is generally negligible, even near the equator, in the boundary-layer momentum balance. The large SST gradients in the subtropics play an important role in forcing rotational and cross-isobaric winds.

1. Introduction

The processes by which sea surface temperature (SST) forces atmospheric circulation are parts of the key elements of ocean–atmosphere interaction. Our current understanding of these processes is acknowledged as a major weakness in the modeling of the coupled ocean–atmospheric system. Over the last decade there have been a considerable number of studies devoted to numerical and observational studies of the atmospheric response to tropical SST anomalies. Many of the modeling studies have been aimed at developing a mechanistic coupled model to simulate and elucidate the physics of the El Niño–Southern Oscillation (ENSO) (e.g., Zebiak and Cane 1987). Such models require a simple mathematical description of the most relevant dynamics and thermodynamics so that the mechanisms can be better understood.

Analogous to the function of the quasigeostrophic model in studying midlatitude dynamics, the shallow-water model provides a fundamental framework for studying dynamical processes of relevance to the tropical atmosphere. Using a linear shallow-water model on an equatorial beta plane, Matsuno (1966) demonstrated free wave solutions, while Gill (1980) showed solutions for steady tropical motion forced by imposed heating. Most of the simple atmospheric models thus far developed for simulating atmospheric response to SST anomalies follow the formulation of Gill (1980), with the diabatic heating being somehow tied to SST. This type of model may be referred to as a Gill-type model (hereafter, Gill model for convenience).

A fundamental premise in the Gill model is that the low-level winds were driven by diabatic heating. With this assumption, the simplest representation was to follow the original speculation by Bjerkness (1969) relating anomalous heating to local surface heat fluxes determined by SST and its anomalies (Zebiak 1982; Philander et al. 1984). The atmospheric diabatic heating, however, is principally caused by latent heat release in penetrative convection for which both the low-level moisture convergence and the local evaporation supply moisture. The diabatic heating is thus essentially a

* School of Ocean and Earth Science and Technology Contribution Number 2899.

Corresponding author address: Dr. Bin Wang, Department of Meteorology, University of Hawaii at Manoa, 2525 Correa Road, HIG 331, Honolulu, HI 96822.

nonlinear process and interacts with the circulation ... profound influence on latent heating and free-atmo-

In subsequent development of the Gill model the convergence feedback has been taken into consideration (Webster 1981) and the anomalous SST forcing was linked to diabatic heating via either directly changing evaporation rate (Zebiak 1986; Weare 1986) or longwave radiational (Newtonian) cooling (Davey and Gill 1987). Seager (1991) refined the Gill model by replacing CISK parameterization with a new scheme in which convective heating is assumed to occur when a lifted air parcel is buoyant relative to its surroundings. In all linear Gill models unrealistically large momentum damping is necessary to yield reasonable solutions. Neelin (1988) showed that a similar model may be formulated in terms of the flow in the tropical boundary layer alone, arguing that the heavy damping commonly used in the Gill model is plausible.

Lindzen and Nigam (1987), on the other hand, proposed a very different perspective on the role of the SST in forcing low-level atmospheric flow. Contrary to the assumption adopted in the Gill model, the Lindzen–Nigam (hereafter denoted as LN) model neglected the role of convective latent heating and assumed that boundary-layer flow is forced by hydrostatically induced pressure gradient forces that result from SST gradients via vertical turbulent mixing of heat and moisture. To obtain realistic strength of the boundary-

spheric circulation. The intertropical convergence zone (ITCZ) is essentially a boundary-layer system that is greatly affected by SST gradients. For a model that simulates total wind field rather than anomalies (e.g., Seager 1991), this may be a critical deficiency because an adequate simulation of the climatological mean state is a prerequisite for simulation of the anomalies. The drawback associated with the absence of the boundary layer has been recognized in several studies of the Gill model (e.g., Zebiak 1986; Seager 1991; Kleeman 1991). The LN model takes into account momentum forcings by the SST gradient, but it cannot properly determine the pressure change at the top of the boundary layer due to neglect of the free atmospheric processes. A common deficiency in both Gill and LN models is the absence of important interactions between the boundary layer and the free atmospheric circulation.

Observational evidence has shown that the structure of ENSO anomalies differs between the western and eastern-central Pacific (Wang 1992). This structural difference was attributed to the east–west contrast of ocean–atmospheric interaction processes in the Pacific. In the western Pacific (a warm pool and large tropical island region), anomalous convection tends to be strongly influenced by the effect of land–sea thermal

cific cold tongue and the western Pacific warm pool. The increase in the degree of freedom in SST forcing allows an active interaction between the boundary-layer flow forced by SST gradient and the free atmospheric flow driven by thermodynamic forcing of the SST. This leads to a more realistic description of the tropical motion without sizable increase in the computational effort. In addition, the model simulates total circulation and convective heating fields. It can be used to investigate both the annual cycle and interannual variations. The model can be solved for the steady-state solution or for time-dependent evolution. Detailed discussion of the model formulation is given in section 2. In terms of the present model the nature and problems of Gill

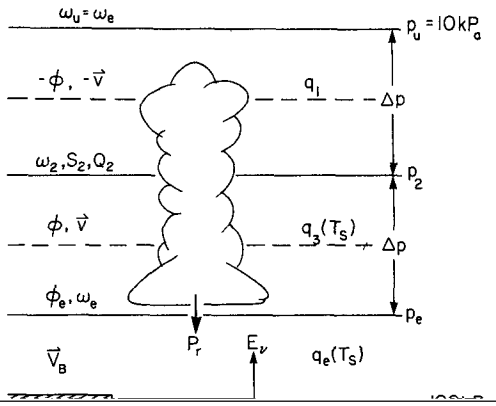

a. The free troposphere

The continuously stratified free troposphere is approximated by a two-level model with the boundary conditions

$$\omega = \omega_e \quad \text{at} \quad p = p_e \tag{2.3a}$$

and

$$\omega = \omega_u \quad \text{at} \quad p = p_u, \tag{2.3b}$$

where ω_e and ω_u are, respectively, the vertical pressure velocity at the top of the boundary layer $p = p_e$ and the tropopause $p = p_u$. For the free troposphere, Rayleigh friction with a coefficient ϵ_* is adopted. Introduce barotropic and baroclinic modes defined, respectively, by

$$\mathbf{V}_+ = \frac{1}{2}(\mathbf{V}_3 + \mathbf{V}_1), \quad \phi_+ = \frac{1}{2}(\phi_3 + \phi_1), \tag{2.4a}$$

and

$$\mathbf{V}_- = \frac{1}{2}(\mathbf{V}_3 - \mathbf{V}_1), \quad \phi_- = \frac{1}{2}(\phi_3 - \phi_1). \tag{2.4b}$$

From (2.1a,b), the barotropic mode satisfies

$$\frac{\partial \mathbf{V}_+}{\partial t} + \beta y \hat{\mathbf{k}} \times \mathbf{V}_+ = -\nabla \phi_+ - \epsilon_* \mathbf{V}_+, \tag{2.5a}$$

$$\nabla \cdot \mathbf{V}_+ + \frac{1}{2\Delta p}(\omega_e - \omega_u) = 0, \tag{2.5b}$$

where $\Delta p = (p_e - p_u)/2$ is the half pressure depth of the free troposphere. In the absence of the boundary layer the barotropic mode is independent of the

$$\omega_2 = \omega_e + \Delta p \nabla \cdot \mathbf{V}_-, \tag{2.6b}$$

$$\frac{\partial \phi_-}{\partial t} + \frac{s_2 \Delta p}{2}\omega_2 = -\frac{R\Delta p}{2C_p p_2}(Q_{p2} + Q_{r2}), \tag{2.6c}$$

where S_2, Q_{p2}, and Q_{r2} denote values of static stability, precipitational, and longwave radiational heating at the middle of the free troposphere, $p = p_2$, respectively. The baroclinic mode, $\mathbf{V}_-$ and ϕ_-, can be construed as the horizontal wind and geopotential perturbation at the lower free troposphere (70 kPa, for example).

It has been shown (Wang 1988) that the moisture equation (2.2a) can be expressed in the present model as

$$P_r = -\frac{b}{g}[\omega_2(\bar{q}_3 - \bar{q}_1) + \omega_e(\bar{q}_e - \bar{q}_3 + \bar{q}_1)] + bE_v, \tag{2.7}$$

where $\bar{q}_e$, $\bar{q}_3$, and $\bar{q}_1$ are vertical mean specific humidities in the boundary layer, the lower, and the upper free-tropospheric layers, respectively. It is assumed, based on Tomasi's (1984) observation, that the absolute humidity decays exponentially with height in the lower troposphere so that (see Wang 1988)

$$\bar{q}_e = q_0 \frac{p_s^m - p_e^m}{m(p_s - p_e)}, \tag{2.7a}$$

and

$$\bar{q}_3 = q_0 \frac{p_e^m - p_2^m}{m(p_e - p_2)}, \tag{2.7b}$$

where p_s, p_e, and p_2 are, respectively, nondimension-

$$q_s(T_s) = q_s(T_r)\left[1 + \frac{L_c}{R_v T_r^2}(T_s - T_r)\right], \quad (2.9)$$

where R_v is the gas constant for water vapor. Inserting (2.7c) and (2.9) into (2.8) leads to

$$E_v = \rho_s C_E V_s K_q (T_s - T_*), \quad (2.10)$$

where coefficient $K_q = 6.95 \times 10^{-4}\,\mathrm{K}^{-1}$ and $T_* = 293.2$ K. Equation (2.10) implies that the evaporation rate increases with increasing SST due to the fact that the difference between the saturation specific humidity at SST and the specific humidity of the surface air increases with SST. Because the empirical relation (2.7c) was used, strictly speaking, (2.10) can be applied only to tropical oceanic regions where SST exceeds 22°C. In a small regions of the tropical Pacific near the South American coast where SST is below 22°C, the evaporation rate may be assumed to be independent of SST and is given by $1.8\, C_E V_s K_q$, because the surface air over cool ocean surface is nearly saturated. Computations, however, indicate that this modification to (2.10) for areas with SST lower than 22°C does not affect the solution appreciably. We therefore apply (2.10) to the entire Pacific domain between 30°N and 30°S.

The precipitational heating rate at p_2 is related to P_r by

$$Q_{p2} = \frac{g}{\Delta p} L_c \delta P_r, \quad (2.11)$$

where δ is a switch-on parameter determined by the sign of P_r and other conditions. In the simplest case of conditional heating $\delta = 1$ when P_r computed from (2.7) is positive and $\delta = 0$ otherwise. Further discussions on the representation of switch-on parameter are deferred to section 4.

The representation of longwave radiational cooling closely follows Davey and Gill (1987). The midtropospheric temperature perturbation (from the basic equilibrium state) is assumed to relax back, via longwave radiation process, to an equilibrium temperature field. The equilibrium temperature is supposed to have the same pattern as SST with a reduced amplitude. This is warranted if the lapse rate between the surface and midtroposphere is spatially uniform. This assumption appears to be consistent, to some extent, with observations. For instance, LN has shown that the distribution of 70-kPa temperature during 1979 summer is similar to that of SST with a reduction in amplitude.

The perturbation longwave radiational heating at level p_2 is thus written as

$$Q_{r2} = \mu C_p\left[\frac{2p_2}{R\Delta p}\phi_- + r(T_s - \bar{T}_s)\right], \quad (2.12)$$

where μ is the reciprocal of the Newtonian cooling time, $-(2p_2/R\Delta p)\phi_-$ is the perturbation temperature at p_2, $(T_s - \bar{T}_s)$ is the deviation of SST from its domain average, and r is the ratio of the equilibrium temperature deviation at p_2 to SST deviation.

Substituting (2.6b), (2.7), (2.10), (2.11), and (2.12) into (2.6c), the thermodynamic equation of the free troposphere reads

$$\frac{\partial \phi_-}{\partial t} + \mu\phi_- + C_0^2\left[1 - \delta\frac{RbL_c(\bar{q}_3 - \bar{q}_1)}{C_p p_2 S_2 \Delta p}\right] \times (\nabla \cdot \mathbf{V}_-) = -\mu\frac{R\Delta p}{2p_2} r(T_s - \bar{T}_s) - C_0^2\frac{\omega_e}{\Delta p}\left(1 - \delta\frac{RbL_c\bar{q}_e}{C_p p_2 S_2 \Delta p}\right) - \delta\frac{RbL_c}{2C_p p_2}\rho_s g C_E V_s K_q (T_s - T_*), \quad (2.13)$$

where

$$C_0^2 \equiv \frac{1}{2} S_2 \Delta p^2, \quad S_2 \equiv S_0\left(\frac{P_s}{P_2}\right)^2. \quad (2.14)$$

In (2.14), C_0 is the gravity wave speed for the gravest baroclinic mode and S_0 is the static stability parameter at the surface. The static stability parameter is assumed to be inversely proportional to the pressure square, which is a good approximation in the troposphere.

b. The mixed boundary layer

Over the vast area of the ocean, monsoonal and trade-wind boundary layer may be treated to be convective. If the turbulent mixing is confined by a stable layer (say, an inversion), the boundary layer may approach a well-mixed state. In most trade-wind region air flows up SST gradient, the boundary layer may be very convective due to surface heating caused by surface sensible and latent fluxes. Under these conditions, the wind does not vary significantly in the vertical and the layer can be treated as a slab (Young 1987). This provides a convenient way to focus on the bulk properties of the boundary-layer flow and the influences from the top and the bottom.

The stress conditions at the bottom ($p = p_s$) and top ($p = p_e$) of the boundary layer are

$$\boldsymbol{\tau} = -\rho_s K_D \mathbf{V}_s, \quad \text{at} \quad p = p_s, \quad (2.15a)$$

$$\boldsymbol{\tau} = 0, \quad \text{at} \quad p = p_e. \quad (2.15b)$$

The first is surface drag. By matching the mixed layer with a surface layer, it can be shown that (e.g., Wang 1988)

$$K_D = \frac{A_z}{h \ln(h/z_0)}, \quad (2.16)$$

where A_z is a constant vertical turbulent coefficient; h and z_0 denote the depth of the surface layer and surface roughness length. Observations indicate that neither

wind speed nor wind direction varies discontinuously with height across the trade inversions (Riehl 1979). Vanishing stress at the top of the boundary layer is thus assumed in (2.15b). With the conditions (2.15a) and (2.15b), the equation of motion for steady flows in the well-mixed boundary layer can be written as

$$\mathbf{k} \times \beta y \mathbf{V}_B = -\nabla\left[\frac{1}{p_s - p_e}\int_{p_e}^{p_s} \phi dp\right] - \frac{\rho_s g K_D}{p_s - p_e}\mathbf{V}_B, \tag{2.17a}$$

$$\omega_e = (p_s - p_e)\nabla \cdot \mathbf{V}_B, \tag{2.17b}$$

where

$$\mathbf{V}_B \equiv \frac{1}{(p_s - p_e)}\int_{p_e}^{p_s} \mathbf{V}\, dp \tag{2.18}$$

represents vertically averaged horizontal wind in the boundary layer. In deriving (2.17a), it was assumed that $\mathbf{V}_s = \mathbf{V}_B$.

Since vertical variation of temperature has little influence on the vertical mean geopotential in the boundary layer, for clarity we assume $T(x, y, p) = T_0(x, y)$ where T_0 denotes air temperature. It can be shown that for ideal gas

$$\frac{1}{(p_s - p_e)}\int_{p_e}^{p_s} \phi dp = \phi_e - RT_0\left[\frac{p_e}{p_s - p_e}\ln\frac{p_s}{p_e} - 1\right], \tag{2.19}$$

and if $p_s - p_e \ll p_e$, the following approximate equation is valid:

$$\frac{1}{(p_s - p_e)}\int_{p_e}^{p_s} \phi dp = \phi_e - \frac{R}{2}\frac{p_s - p_e}{p_e}T_0, \tag{2.20}$$

where ϕ_e denotes the geopotential at the top of the boundary layer. Thus, the boundary-layer momentum equation is

$$\mathbf{k} \times \beta y \mathbf{V}_B = -\nabla\phi_e + \frac{R}{2}\frac{(p_s - p_e)}{p_e}\nabla T_s - \frac{\rho_s g K_D}{p_s - p_e}\mathbf{V}_B, \tag{2.21}$$

where we have assumed that the gradient of the surface air temperature, ∇T_0, is equal to the SST gradient, ∇T_s.

c. *Nondimensional equations*

For convenience, we scale horizontal velocity $\mathbf{V}_-$ and $\mathbf{V}_B$ by C_0, geopotential ϕ by C_0^2, time t by $(\beta C_0)^{-1/2}$, horizontal coordinates x, y, by $(C_0/\beta)^{1/2}$, and the temperature by C_0^2/R. The nondimensional governing equations for the motions in the present coupled free atmosphere–boundary layer model are derived from (2.6a), (2.13), (2.17b), and (2.21):

$$\frac{\partial}{\partial t}\mathbf{V} + y\mathbf{k} \times \mathbf{V} = -\nabla\phi - \epsilon\mathbf{V}, \tag{2.22a}$$

$$\frac{\partial}{\partial t}\phi + N\phi + (1 - \delta I)\nabla \cdot \mathbf{V} = -NG(T_s - \bar{T}_s) + d(\delta B - 1)\nabla \cdot \mathbf{V}_B - \delta F|\mathbf{V}_B|(T_s - T_*), \tag{2.22b}$$

$$-y\mathbf{k} \times \mathbf{V}_B = -\nabla\phi + A\nabla T_s - E\mathbf{V}_B. \tag{2.22c}$$

For simplicity, subscript "−" in (2.22) was dropped; thus, ϕ and $\mathbf{V}$ now represent the nondimensional geopotential and horizontal velocity in the lower free troposphere. To be consistent with the two-level approximation of the free atmosphere, the geopotential gradient at the top of the boundary layer should be equal to that at the lower level of the free troposphere; that is, $\nabla\phi_e = \nabla\phi$. Nine nondimensional parameters in (2.22) are

$$\epsilon = \frac{\epsilon_*}{\sqrt{\beta C_0}} \quad \text{Rayleigh friction coefficient} \tag{2.23a}$$

$$N = \frac{\mu}{\sqrt{\beta C_0}} \quad \text{Newtonian cooling coefficient} \tag{2.23b}$$

$$I = \frac{RL_c b}{C_p P_2 S_2 \Delta p}(\bar{q}_3 - \bar{q}_1) \quad \text{Heating coefficient due to free-troposphere moisture convergence} \tag{2.23c}$$

$$B = \frac{RL_c b}{C_p P_2 S_2 \Delta p}\bar{q}_e \quad \text{Heating coefficient due to boundary-layer moisture convergence} \tag{2.23d}$$

$$G = \frac{\Delta p}{2p_2}r \quad \text{Coefficient of longwave radiational forcing} \tag{2.23e}$$

$$d = \frac{p_s - p_e}{\Delta p} \quad \text{Depth of the boundary layer} \tag{2.23f}$$

$$F = \left(\frac{C_0}{\beta}\right)^{1/2}\frac{\rho_s g L_c b}{2C_p p_2}C_E K_q \quad \text{Coefficient of evaporation forcing} \tag{2.23g}$$

$$A = \frac{p_s - p_e}{2p_e} \quad \text{Coefficient of SST gradient forcing} \tag{2.23h}$$

$$E = \frac{\rho_s g K_D}{(p_s - p_e)\sqrt{\beta C_0}} \quad \text{Ekman number of the boundary layer} \tag{2.23i}$$

The model contains a number of key parameters, which are listed in Table 1. The values shown in Table 1 are used in the computation unless otherwise stated. The value of K_D in Table 1 is computed from (2.16), assuming a vertical turbulent mixing coefficient $A_z = 10$ m^2 s^{-1}, a depth of the surface layer $h = 50$ m, and a surface roughness length $z_0 = 1$ cm. Other constants

TABLE 1. Basic parameters and their values used in the present model.

Symbol	Parameter	Standard value
S_0	Static stability parameter at the surface, Eq. (2.14).	0.75×10^{-6} m^2 s^{-2} Pa^{-2}
p_e	Pressure at the top of the boundary layer, Eq. (2.3a).	85 Kpa
H_1	Water vapor density scale height, Eq. (2.7).	2.2 Km
b	Efficiency of condensation heating, Eq. (2.2a).	0.75
r	Ratio of the equilibrium temperature deviation at the midtroposphere to SST deviation, Eq. (2.12).	0.6
ϵ_*	Rayleigh friction coefficient, Eq. (2.5a).	10^{-5} s^{-1}
μ	Newtonian cooling coefficient, Eq. (2.12).	10^{-5} s^{-1}
C_E	Coefficient of turbulent vertical moisture flux, Eq. (2.8).	1.5×10^{-3}
K_D	Surface friction coefficient, Eqs. (2.15a), (2.16).	2.3×10^{-2} m s^{-1}

used in the model include surface pressure, $p_s = 100$ kPa; pressure at the top of the free troposphere, $p_u = 10$ kPa; air density in the boundary layer, $\rho_s = 1.22$ kg m^{-3}; density scale height, $H \equiv 7.8$ km; mean specific humidity at the upper-tropospheric layer, $\bar{q}_1 \equiv 4 \times 10^{-4}$; and $T_* \equiv 293.2$ K. Once p_e is given, $\Delta p = (p_e - p_u)/2$ and $p_2 = p_e + \Delta p$ are known. The static stability parameter at p_2, S_2, and the gravity wave speed of the gravest baroclinic mode C_0 can be calculated from (2.14). For $p_e = 90$ kPa, $S_2 = 3.14 \times 10^{-6}$ m^2 s^{-2} Pa^{-2} and the corresponding value of C_0 is 50 m s^{-1}.

d. Numerical procedure and data

Equations (2.22a–c) can be readily combined into a single equation in terms of the low-level free-troposphere geopotential height, ϕ; that is,

$$N\phi + (1 - \delta I)L_\epsilon(\phi) - d(\delta B - 1)L_E(\phi) = Ad(\delta B - 1)L_E(T_s) - GN(T_s - \bar{T}_s) - \delta FV(T_s - T_*), \quad (2.24)$$

where

$$L_\epsilon = -\epsilon \frac{\partial_{xx} + \partial_{yy}}{\epsilon^2 + y^2} + 2y \frac{\epsilon\partial_y - y\partial_x}{(\epsilon^2 + y^2)^2}, \quad (2.24a)$$

$$L_E = -E \frac{\partial_{xx} + \partial_{yy}}{E^2 + y^2} + 2y \frac{E\partial_y - y\partial_x}{(E^2 + y^2)^2}, \quad (2.24b)$$

and for simplicity, V denotes the averaged surface wind speed. Equation (2.24) can be cast into a canonical form of nonhomogeneous elliptic equation.

Equation (2.22) or (2.24) was then written in a finite-difference form with lateral boundary conditions that require the gradients of dependent variables to vanish in the normal direction of boundaries. The grid space is 2° in latitude and 5° in longitude. The model is forced by surface temperature within 32°N and 32°S from 115°E to 65°W. Two methods were used to solve the derived difference equations: iterative matrix inversion and time integration. In the simplest case in which all coefficients are linearized, the difference equation derived from (2.24) is solved using direct matrix inversion. In general, iterative matrix inversion is needed because some of the coefficients are dependent on motion; for instance, the condensational heating depends on precipitation and the evaporation rate depends on variable wind speed. In the most complicated case, the depth of the boundary layer is designed to be dependent on motion, and thus, almost all coefficients become motion dependent. Time integration is necessary in order to obtain steady solutions in this complicated case. Two approaches are also used to verify the accuracy against each other.

Climatological monthly mean fields of SST, sea level pressure, and surface winds derived from COADS for the period 1900–1979 by Sadler et al. (1987) were used. Monthly mean of highly reflective cloud (HRC) data (Garcia 1985) is used as an indirect measurement of precipitation. According to our regression study, a monthly mean of HRC of 3 day mo^{-1} corresponds approximately to a rainfall rate of 210 mm mo^{-1}. A deviation of HRC of 1 day mo^{-1} corresponds to a deviation in rainfall rate of about 80 mm mo^{-1}. Figure 2 presents January mean fields of SST, sea level pressure, surface winds, and HRC. The SST over the land area is interpolated. A more realistic representation of land surface temperature is given in Fig. 8. The surface temperature is used as forcing, and other fields are used to evaluate the model simulations.

3. Interpretation of the Gill and Lindzen–Nigam models

a. The Gill model

In the absence of boundary layer, that is, $p_e = p_s$, and for a steady motion, (2.22a,b) reduces to

$$\epsilon\mathbf{V} + y\mathbf{k} \times \mathbf{V} = -\nabla\phi, \quad (3.1a)$$

$$N\phi + (1 - \delta I)\nabla \cdot \mathbf{V} = -NG(T_s - \bar{T}_s) - \delta FV(T_s - T_*), \quad (3.1b)$$

where $V = 5$ m s^{-1} is used to represent domain-averaged surface wind speed. The switch-on parameter $\delta = 1$ if precipitation is positive, and $\delta = 0$ otherwise. Equations (3.1a,b) are equivalent to those of Davey and Gill (1987) after dropping off the second term

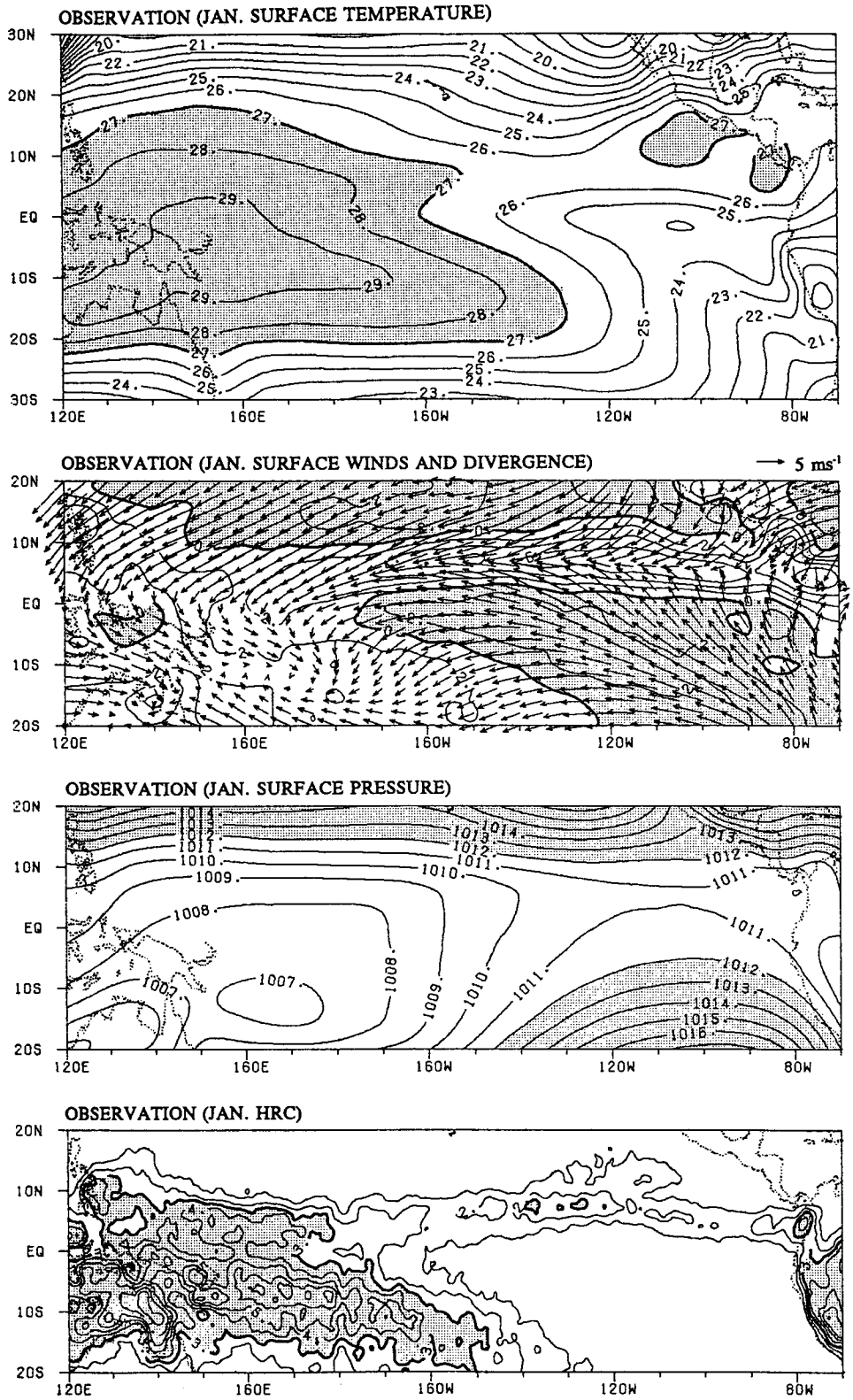

FIG. 2. Observed January mean SST (in units °C), surface winds and divergence (in units of 10^{-6} s^{-1}), sea level pressure, and the number of days with highly reflective cloud (HRC). The SST, surface winds, and pressure data are from COADS climatology derived by Sadler et al. (1987). The HRC data are derived from visible and infrared satellite mosaics by Garcia (1985).

(evaporational forcing) in the rhs of (3.1b) and equivalent to those of Zebiak (1986) or Weare (1986) upon neglecting the first term (longwave radiational forcing) in the rhs of (3.1b) with the exception that (3.1) applies to the total motion rather than anomaly field. The latent heat release associated with free-troposphere moisture convergence in a single vertical-mode model acts simply to reduce the static stability. As a result, the nondimensional effective static stability decreases from 1 to $1 - I$ in the region of latent heat release. Given the empirical relation between specific humidity and SST, (2.7a,b,c), the condensational heating coefficient I is always less than 1 unless SST exceeds 31°C (if $P_u = 10$ kPa and the water vapor density scale height $H_1 = 2.2$ km are used). This implies that we are dealing with a large-scale stable regime of the moist atmosphere.

The Gill model, as expressed by (3.1), involves five parameters (ϵ, N, I, G, and F). When r and C_E take values listed in Table 1, the coefficients of longwave radiational (G) and evaporational (F) forcings are fixed. To be consistent with Zebiak (1986) and Davey and Gill (1987), the condensation heating coefficient, I, is assumed to be a constant ($I = 0.78$). In previous Gill-type models the Rayleigh friction and Newtonian cooling time scale were taken to be the same. The solution of (3.1) is known to be sensitive to the magnitude of the damping. The best agreement between model results and observations in all cases requires large values of damping coefficient ($\sim 10^{-5}$ s^{-1}), corresponding to a decay time of about 1 1/4 day (Fig. 3a).

We now examine the sensitivity of the solution to each of the thermal and mechanical damping, respectively. If the thermal damping is reduced by a factor of 5 (corresponding to a Newtonian cooling time of

cient, μ. For strong thermal damping, $\mu = 10^{-5}$ s^{-1}, the resultant low-level winds due to longwave radiational forcing are generally stronger than those due to evaporational forcing by a factor of 3 to 4 (figures are not shown). This agrees with Kleeman's (1991) assessment. However, for smaller Newtonian cooling coefficients, $\mu = 2 \times 10^{-6}$ s^{-1}, for instance, the forced motion due to each forcing term in the rhs of (3.1b) alone is comparable in amplitude (figures are not shown); that is, the evaporational forcing is as important as longwave radiational forcing. It follows that in the presence of large thermal damping ($\mu \sim 10^{-5}$ s^{-1}), the longwave radiational forcing of SST is much more effective than the evaporational forcing; only when the thermal damping is small ($\mu \sim 10^{-6}$ s^{-1}) will the solution be sensitive to the evaporational forcing. If a large thermal damping is used while the radiational forcing is absent as the case in the Zebiak model, a large evaporational forcing must be employed in order to obtain a realistic magnitude of wind field. This should not be viewed as a serious problem because the thermal damping can be reduced by an order of magnitude, and thus, a realistic evaporational forcing can yield a reasonable solution. Figure 3d presents such a solution.

In the Gill model, the South Pacific convergence zone (SPCZ) is simulated reasonably well, albeit the intensity is slightly weak. The trade winds are also roughly captured, yet the meridional wind components are too small. The major drawback of the Gill model is the failure in reproducing the ITCZ in the central Pacific. The observed convergence in the ITCZ is three times stronger than that in the SPCZ, yet the simulated convergence in the ITCZ is much weaker than that in the SPCZ. Since anomalous heating is dependent on

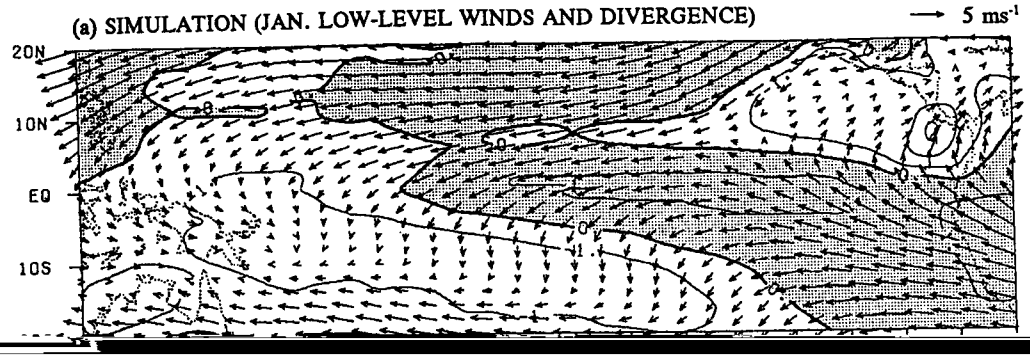
(a) SIMULATION (JAN. LOW-LEVEL WINDS AND DIVERGENCE)
5 ms-1
20N
10N
EQ
10S

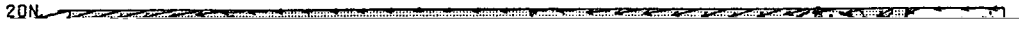
20N

top of the boundary layer, which in the present model is equal to the perturbation geopotential of the lower free troposphere; H_0 and H represent the depth of the boundary layer and the density scale height, respectively. For the convenience of comparison with the LN model, in deriving (3.3a,b) the atmosphere has been treated as Boussinesq fluid so that $p_s - p_e = \rho_s g H_0$, $p_e = 2\Delta P = \rho_s g H$, and T_0 is the mean air temperature.

Equations (3.3a,b) are equivalent to those of the LN model. In fact, the equations of motion in the LN model written on an equatorial beta plane, z coordinates with some of the smaller terms neglected for the sake of clarity, are (e.g., see Neelin 1989)

$$\epsilon \mathbf{V}_B + \beta y \mathbf{k} \times \mathbf{V}_B = -\nabla \phi_e + \frac{gH_0}{2T_0} \nabla T_s, \quad (3.4a)$$

$$\epsilon_T \phi_e + gH_0 \nabla \cdot \mathbf{V}_B = 0, \quad (3.4b)$$

where the Rayleigh friction coefficient is equivalent to (K_D/H_0) in (3.3a) and ϵ_T is interpreted as the reciprocal of the time scale during which cumulus mass fluxes associated with boundary-layer convergence reach a steady state. Notice that the momentum equations (3.3a) and (3.4a) are identical and Eqs. (3.3b) and (3.4b) are also identical if

$$\mu = 2 \frac{C_0^2}{C^2} \epsilon_T \quad (3.5)$$

is satisfied, where $C = (gH)^{1/2}$ is the gravity-wave speed of the equivalent barotropic mode. Typical values for C_0 and C are 50 and 280 m s^{-1}, respectively, and the ratio $2C_0^2/C^2 = 1/16$.

One question with the LN model is how to interpret the pressure adjustment equation (3.4b). Lindzen and Nigam (1987) assume that convection acts as a device to vent convergent air mass out of the boundary layer, so that geopotential perturbation at the top of the boundary layer can be generated through a time scale of half an hour or so. The present model provides an alternative physical interpretation to the pressure adjustment equation of the LN model. Equation (3.3b) implies a balance between the adiabatic warming associated with the boundary-layer divergence and the longwave radiational cooling with a time scale $(1/\mu)$ of eight hours or so. For instance, near the equator where the Coriolis force nearly vanishes, the boundary-layer flows converge into the region of high SST due to the momentum forcing of SST [Eq. (3.3a)]. The convergent flows induce adiabatic cooling at the top of the boundary layer and an increase in the geopotential [Eq. (3.3b)]. The latter offsets the effect of the momentum forcing of SST, suppressing unrealistically large divergence. Since (3.3b) is derived from the heat equation, it is also instrumental for understanding the short time scale required in the LN model. The pressure adjustment equation in the LN model can be viewed as an oversimplified thermal balance because all diabatic heating processes and the vertical motion in the free troposphere are omitted. When complex thermodynamic processes are crudely parameterized in terms of such a simple balance relation, in order to obtain reasonable resultant pressure adjustment the parameter μ (or ϵ_T) has to be tuned at the expense of losing reality.

To elaborate this point we first examine the strength of the boundary-layer flows forced by the SST gradient for given reasonable values of forcing parameter (A). Figure 4a presents the flows simulated by the LN model using observed January climatological SST field and assuming $K_D = 2.3 \times 10^{-2}$ m s^{-1}, $\mu = 10^{-5}$ s^{-1}, and boundary-layer depth of about 1 km. The magnitude of the simulated wind speed is O(1 m s^{-1}), nearly five times smaller than the observed or that simulated by the Gill model (Figs. 2a and 3a). This can be better understood if the LN model is transformed into a Gill-type model. As in Neelin (1989), let

$$\tilde{\phi} = \phi - A(T_s - \bar{T}_s). \quad (3.6)$$

Equations (3.2a,b) become

$$E\mathbf{V}_B - y\mathbf{k} \times \mathbf{V}_B = -\nabla \tilde{\phi}, \quad (3.7a)$$

$$N\tilde{\phi} + d\nabla \cdot \mathbf{V}_B = -NA(T_s - \bar{T}_s). \quad (3.7b)$$

This is formally equivalent to the Davey–Gill model with a linear heating. When $E \sim \epsilon$, $1 - I \sim d$, one anticipates that the low-level flow in the Davey–Gill model should be comparable with the boundary-layer flow in the LN model if the forcing terms in the rhs of (3.1b) and (3.7b) are comparable. Since

$$\frac{G}{A} = \frac{rp_e}{(P_s - P_e)} \gg 1, \quad (3.8)$$

if the atmosphere were forced by the same SST field, the Davey–Gill model would result in a much stronger wind field than the LN model. This indicates that the momentum forcing of SST in a boundary layer with a depth of about 1 km is too weak to yield a wind field with comparable amplitude as that in the Davey–Gill (1987) model.

The most efficient way to increase the strength of the boundary-layer flow in the LN model is to increase the depth of the boundary layer, because the momentum forcing of SST increases while the friction decreases, both linearly, with increasing boundary-layer depth. Figure 4b shows the wind field computed from the LN model with $H_0 = 3$ km, which is indeed much stronger than that for $H_0 = 1$ km, especially in the vicinity of the equator. However, due to the sharp reduction in frictional force, the cross-isobaric wind component diminished markedly and the boundary-layer winds become more zonal. The corresponding divergence field displays larger discrepancies with the observation. For example, the relatively large convergence over the Maritime Continent is at odds with observation. The only remedy with the simple thermal

balance (3.4b) is to tune Newtonian cooling (or the cumulus adjustment) time scale to modify the feedback-pressure field. Proper choice of the value for μ becomes critical. When a Newtonian cooling time of about eight hours (or equivalently, a cumulus adjustment time of one half hour) is used, the solution is in best agreement with observations (Fig. 4c). Thus, in the absence of diabatic heating, a deep boundary layer of 3 km and a restrictive value of cumulus adjustment time are necessary to obtain reasonably realistic winds and convergence, as employed in LN.

c. *The present model*

In view of the aforementioned deficiencies, to better simulate tropical low-level circulation and precipitation, the dynamics of both the Gill and LN models needs improvement. In this regard, a combination of

boundary-layer and free-troposphere physics is the key. Presented in Fig. 5 are January mean fields simulated

friction. It is interesting to note that the SPCZ is weaker and broader as well as substantially deeper than the

using the present model in which p_e = 850 mb. In order to compare with the results of Gill and LN models

ITCZ. It can be recognized in both the boundary layer and the low-level free troposphere. This is probably the

boundary-layer flows no longer critically depend upon the magnitude of thermal damping because a full heat equation (2.22b) is used rather than the oversimplified version (3.2b). In fact, even when μ reduces to 2×10^{-6} s^{-1}, the resultant boundary-layer flows (see Fig. 5c) bear close resemblance to those in Fig. 5b. Another feature in the present model is that moisture distribution is a function of SST, so that nondimensional condensational coefficients I and B increase with SST. As a result, the moisture effect gains importance in high SST regions, especially as the parameter I approaches the critical value unit. This enhances the condensational heating in high SST region that feeds back to circulation, resulting in lower surface pressure and stronger precipitation.

4. Heating parameterization schemes

The description of the thermodynamic processes has been recognized as a major weakness of the simple models, and much effort has been made in this regard (e.g., Zebiak 1986; Seager 1991; Kleeman 1991).

Given the fact that the moisture supply to penetrative convection is primarily provided by low-level convergence, a key element of the heating parameterization is to deal with the interaction between latent heating and moisture convergence. This was the theme of CISK (conditional instability of the second kind) type of cumulus parameterization (Charnev and Eliassen 1964; heating normally requires the existence of low-level convergence so that the second prerequisite is taken into account. The first condition, however, is not automatically satisfied everywhere in the tropics and should be considered in the parameterization. As the simplest device to include the first condition, we may add an additional requirement for the occurrence of convection in terms of a threshold SST. The idea invoked here is that the conditionally unstable stratification depends on high humidity in the boundary layer that increases with SST. Using monthly mean data, Graham and Barnett (1987) concluded that deep convection occurs in regions where underlying SST exceeds 28°C. This suggests that a critical SST may be required in order for the atmosphere to be conditionally unstable. Upon the implementation of this condition, we specify that

$$\delta = \begin{cases} 1, & \text{if} \quad T_s \geq 301 \text{ K}, \quad P_r > 0, \\ 0, & \text{otherwise.} \end{cases} \tag{4.2}$$

Kleeman (1991) has independently proposed a similar scheme in a Gill-type anomaly model. He used a moist static energy criterion for deciding occurrence of the anomalous convective heating, which is in essence tantamount to a threshold SST criterion.

4) *SST-dependent conditional heating.* In a statistical sense, the time-averaged degree of conditional in-

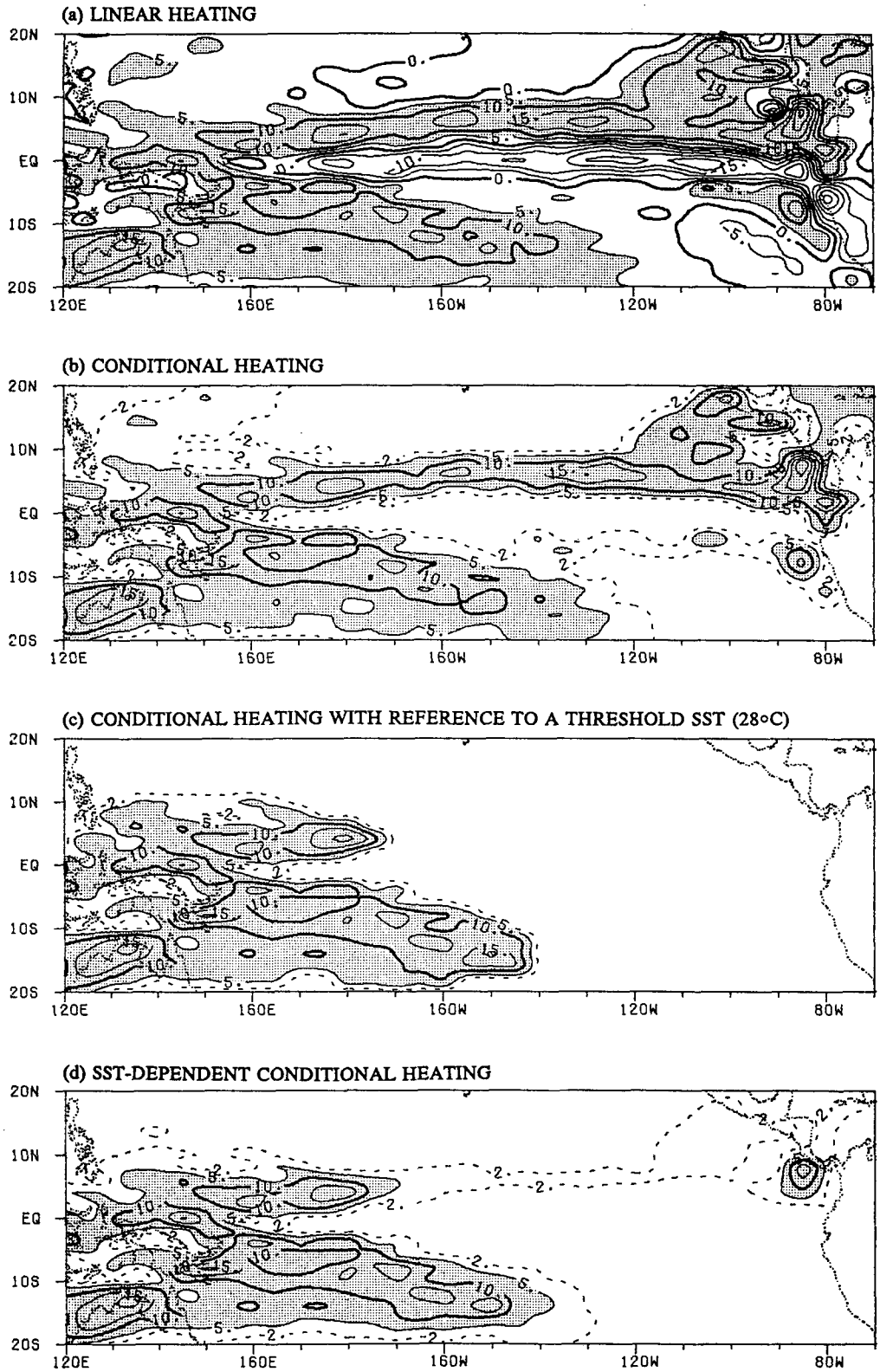

FIG. 6. January mean precipitation rate (in units of mm/day) simulated by the present model with a scheme of (a) linear heating, (b) conditional heating, (c) conditional heating with reference to a threshold SST, and (d) general SST-dependent conditional heating.

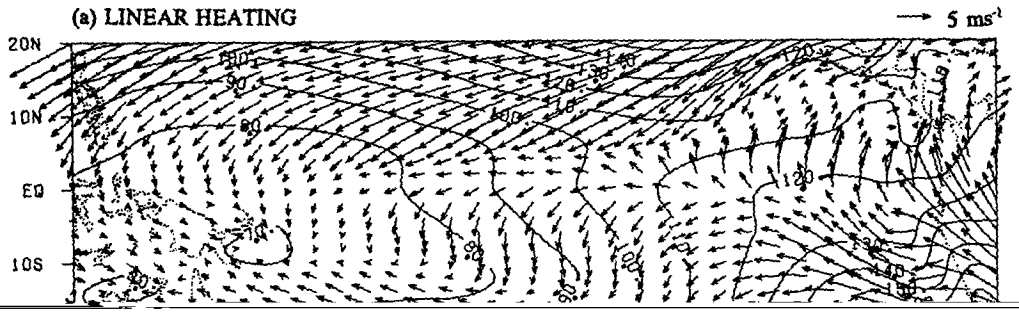
(a) LINEAR HEATING
5 ms-1
20N
10N
EQ
10S


(b) CONDITIONAL HEATING
5 ms-1

itive precipitation only, the changes in the western Pacific wind field are minimal, whereas the unrealistic negative precipitation and associated cooling in the trade-wind divergent regions are removed. The amplitude of the trades decreases accordingly, and the precipitation is more concentrated in a narrow band along the ITCZ (Fig. 6b). Although the convergence in the ITCZ is stronger than that in the SPCZ by a factor of 2 or 3, the precipitation rates in the ITCZ and SPCZ are comparable due to the fact that the low-level humidity is higher and the low-level convergent layer is deeper in the SPCZ than in the ITCZ. The precipitation pattern is significantly improved after replacing linear heating with a conditional heating. Compared with the observed rate of occurrence of HRC (Fig. 2d), however, the precipitation rate over the ITCZ is apparently overestimated. Applying an additional threshold SST = 28°C to control the switch-on of heating results in a complete removal of precipitation in the eastern Pacific (Fig. 6c), which underestimates ITCZ rainfall. On the other hand, when the SST-dependent conditional heating [Eq. (4.3)] is employed, a weaker precipitation rate occurs in the ITCZ (Fig. 6d), although the strength is substantially reduced compared to the case of conditional heating without SST dependence. This rainfall pattern is favorably comparable with observed HRC distribution (Fig. 2d). The reduction in precipitation rate in the eastern Pacific is accompanied by a corresponding weakening of the near-equatorial trough, resulting in a decrease in the amplitude of the southeast trade winds because the pressure gradient between the equatorial trough and subtropical highs abates.

Betts (1982) and Emmanuel (1986) have questioned whether the tropical atmosphere is in the mean conditionally unstable. An alternative thought proposed in their studies is that buoyancy acts as the forcing for convection, whereas neither high humidity nor moisture convergence in the boundary layer is required for the occurrence of convection. Based upon this proposition, Seager (1991) formulated a heating scheme in which convection was parameterized with reference to buoyancy, and the heating in regions of convection was computed using the cloud model of Yanai et al. (1973). The resultant rate of convective heating, however, remains proportional to the precipitation rate, a the underlying SST, the higher the equivalent potential temperature in the boundary layer.

To facilitate comparison, the present model was reduced to a Gill model by removal of the boundary layer with all parameters taking the same values as in Seager (1991) except that the heating is the modified CISK scheme with reference to a threshold SST. The results are comparable with those shown in Fig. 3b of Seager (1991), indicating that the two different schemes give similar results in terms of function, if not interpretation.

5. Effects of land–sea thermal contrast and other physical processes

In this section we assess the impacts of various physical processes on the solution in terms of controlled experiments or diagnostic analysis of observed data. The heating scheme used is the SST-dependent conditional heating [Eq. (4.3)].

a. The influences of parameterized land surface processes

The temperature and evaporation efficiency differ between the ocean and land surface due to different heat capacity and moisture conditions. This thermal contrast sharpens with increasing latitude. To qualitatively identify the impact of the land–ocean thermal contrast, we inserted an idealized land surface temperature distribution over the South and North American continents within the present forcing domain. The land surface temperature is assumed to be a function of latitude only. The latitudinal dependence is specified with reference to observed temperature. The land surface temperature is then merged smoothly with adjacent SST field. The resultant surface temperature is presented in Fig. 8a. The efficiency coefficient of condensation, b, is reduced by 30% over Australia to account for the effect of the local dry conditions.

With the foregoing land effects included, the precipitation over South America and Australia is much improved. This can be readily seen from comparison of Fig. 8c with Figs. 2d and 6d. The pressure and wind fields near the landmass also exhibit drastic changes

The circulation changes over and in the vicinity of Australia are also noticeable. Comparison of Fig. 6d and Fig. 8c reveals that the rainfall and convergent circulation in the western part of the SPCZ and Maritime Continent are sensitive to the change of moisture condition over Australia. Changing surface temperature in Australia further enhances the low pressure in northwest Australia and associated monsoonal westerlies over the Arafura Sea (not shown). This appears to support the results by Kiladis et al. (1989), who found, by general circulation model (GCM) experiments, that removal of the Australian continent destroys the Southern Hemisphere monsoon and undermines the western part of the SPCZ.

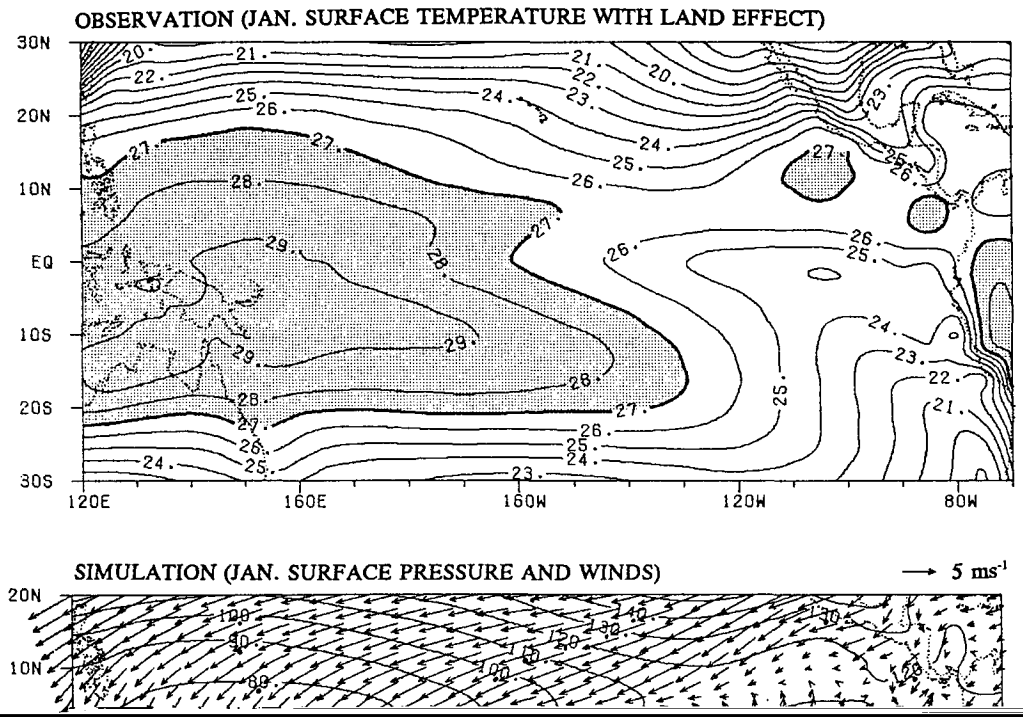

It is of interest, however, to observe that the changes in land surface temperature mainly affect circulations nearby and exert little influence on remote oceanic regions (e.g., the ITCZ and the eastern portion of the SPCZ from 160°E to 130°W). This is evident by comparing the precipitation pattern in Figs. 6d and 8c and the winds in Figs. 7d and 8b. It is suggested that the existence of the ITCZ and SPCZ does not depend upon the land–ocean thermal contrast, albeit the strength of the SPCZ near New Zealand is affected by the land effects over Australia.

While direct thermal effects of the continents contribute little to the formation of the oceanic convergence zones, the South American continent provides a boundary condition for the Pacific basin that supports coastal upwellings, cold currents, and reflects Rossby waves. These, along with the equatorial upwelling, maintain the prominent eastern Pacific cold tongue and large zonal and meridional SST gradients that are responsible for the formation of the oceanic convergence zones. In this sense, the continents, especially the South American continent, indirectly contribute to the origin of the ITCZ and SPCZ.

b. The role of nonlinear advection of momentum

Figure 9 illustrates the relative magnitudes of each of the terms of the following horizontal momentum equation computed using observed January mean sea level pressure and wind data derived by Sadler et al. (1987):

$$\mathbf{V}_B \cdot \nabla \mathbf{V}_B - \beta y \mathbf{k} \times \mathbf{V}_B = -\frac{1}{\rho} \nabla P_s + \mathbf{F}_r. \quad (5.1)$$

The friction is calculated as a residual, which includes transient-eddy effects on the time means. The latter are unknown and assumed to be small in view of the steadiness of the trades. The Coriolis force is the same order of magnitude as the pressure gradient force in the tropics except near the equator between about 3°N and 3°S (Fig. 9b). The normalized friction reaches maximum near the equator, where it is comparable with the pressure gradient force and decreases poleward, yet remains the same order of magnitude as the Coriolis force and pressure gradient force (Fig. 9c). The nonlinear advection term is small almost everywhere except in a narrow band located south of the equator and north of the SPCZ between 160°E and 170°W, where its magnitude reaches about one-third of the pressure gradient force or other two terms (Fig. 9d). It is concluded that the nonlinear advection of momentum plays a minor role in the dynamics of the Pacific boundary layer. The basic balance lies between friction and pressure gradient force near the equator and among the pressure gradient force, Coriolis force, and friction outside of the equatorial oceanic waveguide. This adds confidence to the usage of a linear boundary-layer model.

In the upper troposphere, the contribution of transient (not only rotational but also divergent transient) eddies to the time-mean flow has been shown to be comparable to the mean flow terms and must be considered (Hoskins 1983; Hoskins and Sardeshmukh 1987). In (2.22a), however, the transient eddy effects are rolled out. In addition, the nonlinear advection terms for the steady motion are also neglected. For steady motion, the neglect of nonlinear terms is reasonable only if the Rayleigh friction dominates the advection of momentum; namely,

$$\epsilon \gg \frac{V}{L},$$

where V and L are, respectively, characteristic horizontal velocity and length scale. For large-scale low-frequency motion, $L \sim 6 \times 10^6$ m and $V \sim 10$ m s^{-1}, the corresponding advective time scale is about one week. The damping time scale required in a linear model should be an order of one day in order to neglect nonlinear terms. Most linear models indeed rely on a large damping coefficient to obtain reasonable results (Gill 1980; Zebiak 1986; and others). In the presence of the boundary layer, large mechanical damping in the free atmosphere remains necessary. Sensitivity tests indicate that when the mechanical damping coefficient in the free troposphere is reduced to an order of 10^{-6} s^{-1}, no steady solution can be achieved. Such a large mechanical damping appears to be necessary for maintaining the momentum balance in a linear model when the transient eddy effects and the advection of momentum by steady flows are absent.

c. The impacts of the depth of the boundary layer

The depth of the boundary layer is an important parameter in the present model. As seen in (2.23), all nondimensional parameters depend, explicitly or implicitly, on the pressure depths of the boundary layer or free troposphere that are functions of p_e, in particular, the boundary-layer parameters (d, A, and E).

Assume all parameters are fixed as in Table 1 except the depth of the boundary layer. Figures 10a,b compare the solutions for p_e = 80 kPa and 90 kPa. There are several prominent differences between Figs. 10a and 10b that are due solely to the change of the boundary-layer depth. When the boundary layer is deeper, the winds near the equator and associated convergence/divergence are substantially enhanced; the trade winds display less meridional components; and the SPCZ shifts equatorward. To interpret these differences it is important to bear in mind that in the present model, the deeper the boundary layer is, the weaker the vertically averaged boundary-layer friction and the stronger the SST gradient–induced pressure gradient forcing [Eq. (2.21)]. In the deeper boundary-layer case, the reduction of friction is responsible for the reduced

(a) PRESSURE GRADIENT FORCE

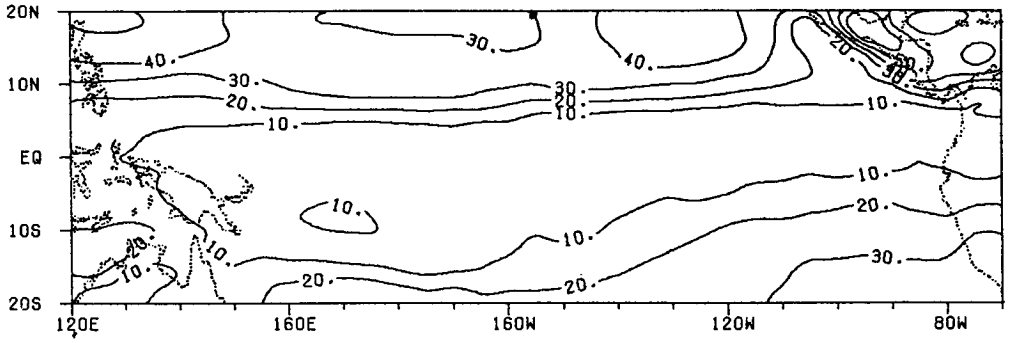

(b) NORMALIZED CORIOLIS FORCE

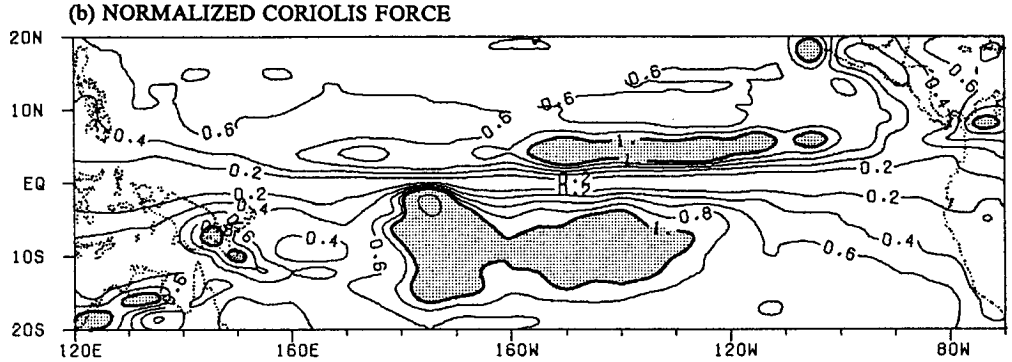

(c) NORMALIZED FRICTION

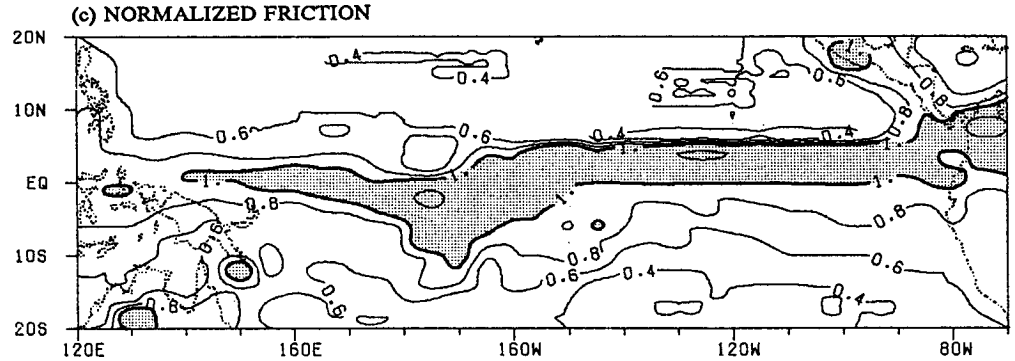

(d) NORMALIZED NONLINEAR ADVECTION

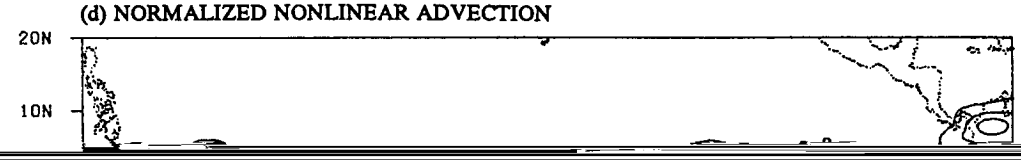

cross-isobaric flow, yielding more zonal trade winds. The increase in pressure force and decrease in friction results in dramatic strengthening of the equatorial zonal winds. Accordingly, the convergence in the equatorial western Pacific is enhanced, resulting in the equatorward shift of the SPCZ. An additional experiment in which the boundary-layer depth is variable (dependent on SST: a lower SST corresponds to a shallower boundary layer) was performed. The change of the boundary-layer depth locally has similar effects on local circulation as those due to the reduction of the vertically averaged friction and the enhancement of the pressure gradients in the boundary layer.

d. The effects of subtropical SST gradient

The results shown in Fig. 10c were obtained when the model was forced by SST between 20°N and 20°S. All other parameters are exactly the same as those used in deriving Figs. 6d and 7d, for which an SST forcing

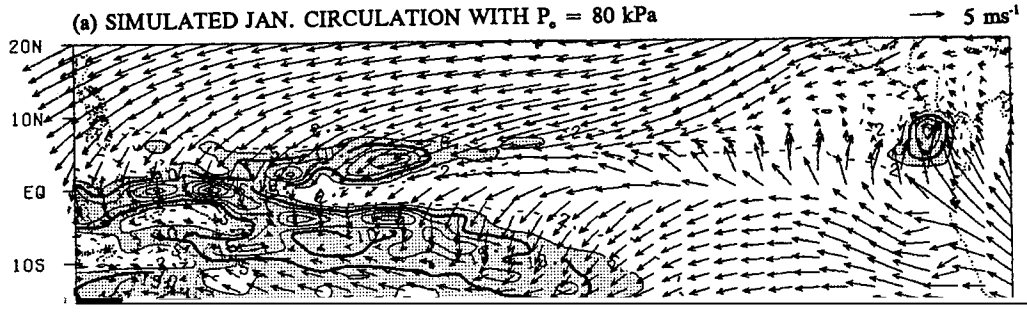

between 32°N and 32°S was used. The differences between the two cases are due to the inclusion (exclusion) of the SST forcing in 20°–32° latitude of both hemispheres. The boundary-layer winds and sea-level pressure near the equator between 10°S and 10°N do not seem to be sensitive to the inclusion of subtropical SST forcing; however, changes in the strength and direction of the trade winds and associated subtropical highs in both hemispheres are obvious. We note that the meridional gradient of SST in subtropical belts between 20° and 32° latitude in both hemispheres is pronounced (greater than 5°C/10° lat) except in the southeast Pacific, where a zonal gradient of SST dominates (Fig. 2a). The large meridional SST gradient reinforces sea level pressure gradient north of 15°N and south of 15°S, causing corresponding increases in the trade-wind speed, the boundary-layer frictional force, and the cross-isobaric component of the wind from high to low pressures (Fig. 7d). The changes in trade winds induce a significant poleward shift of the SPCZ. This experiment suggests that the meridional SST gradient in the subtropics plays an important part

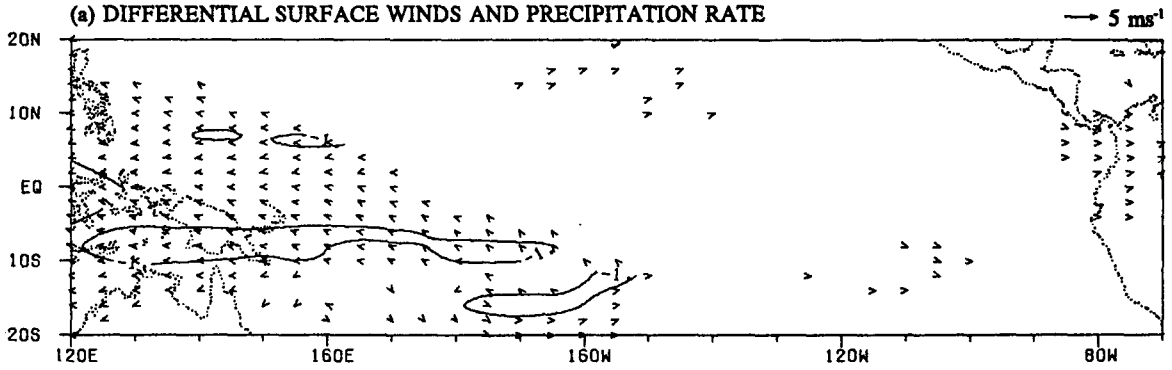

in maintaining the strength of the rotational and cross-isobaric winds.

e. The role of the free-troposphere barotropic mode

In the model formulation presented in section 2, the free-troposphere barotropic mode was intentionally excluded so that the free troposphere is represented by a single baroclinic mode. We now assess the validity of this approximation. To include the barotropic mode interacting with the baroclinic mode, it will suffice to assume $\omega_u = 0$ in the boundary condition (2.3). The resultant nondimensional governing equations for the barotropic mode are

$$\frac{\partial \mathbf{V}_+}{\partial t} + y\mathbf{k} \times \mathbf{V}_+ = -\nabla \phi_+ - \epsilon \mathbf{V}_+, \qquad (5.2a)$$

$$\nabla \mathbf{V}_+ = -2d\nabla \mathbf{V}_B, \qquad (5.2b)$$

while the nondimensional governing equations for the free-troposphere baroclinic mode and boundary-layer flow are the same as (2.22a,b,c) except that 1) the coefficient $(\delta B - 1)$ in (2.22b) should be replaced by $(\delta B' - 1/2)$, where

$$B' = \frac{RL_c b}{C_p P_2 S_2 \nabla P}\left[\bar{q}_e - \frac{\bar{q}_3 + \bar{q}_1}{2}\right], \qquad (5.3)$$

and 2) the term $-\nabla\phi$ in (2.22c) should be replaced by $-\nabla(\phi + \phi_t)$.

Numerical computations based on the upper boundary condition $\omega_u = 0$ were carried out. Figure 11a displays the differences in boundary-layer winds and precipitation rate between the solutions obtained using models with and without the barotropic mode. It is obvious that inclusion of the barotropic mode does not affect the solution appreciably, suggesting that the barotropic mode plays a minor role in determining boundary-layer winds and precipitation. The amplitude and the gradient of the geopotential fluctuation associated with the barotropic mode are an order of magnitude smaller than those of the baroclinic mode (Fig. 11b,c). It follows that to the lowest-order approximation the contribution of the barotropic mode to changes of the geopotential at the top of the boundary layer can be neglected, as is the influence of the barotropic mode on the boundary-layer moisture convergence. This implies that neglect of the weak coupling between the two free-troposphere modes is valid as long as the lowest-order solution is of concern.

6. Summary

Simple atmospheric models are designed to describe only essential physics that is necessary and sufficient for reproducing fundamental features of the observed circulation.

Efforts have been made in formulating the present models by coupling a Gill-type free troposphere with a Lindzen–Nigam boundary layer. A schematic diagram illustrating how SST drives the atmosphere in the present model is given in Fig. 12 that supplements the following discussion. In the boundary layer, SST gradient induces pressure gradient via vertical turbulent transport of surface heat fluxes and hydrostatic balance. The resultant pressure gradient force drives boundary-layer flows whose convergence supplies moisture to convection. Sea surface temperature also directly controls the rate of diabatic heating in the free troposphere via a number of processes (convective heating, longwave radiational cooling, and evaporation) and via affecting the horizontal distribution of moist static energy. The latent heating released in the free-tropospheric convection forces free-tropospheric circulation and changes the boundary-layer pressure. The latter feeds back to the boundary-layer flows. A key simplification in the formulation is the exclusion of the free-troposphere barotropic mode from the model physics. It is demonstrated that the neglect of the weak coupling between the baroclinic and barotropic modes does not affect the lowest-order solution. The present model allows active interplay between the gravest baroclinic mode in the free troposphere, which is stimulated by various thermal forcings of SST, and the boundary-layer flow that is driven directly by the momentum forcing associated with SST gradient. The interplay is effective through their divergent components that control convective latent heat release. This process is an integral part of the essential physics for simulating Pacific basin–wide low-level circulations. The model is capable of reproducing the shallow boundary-layer system, the ITCZ, and much deeper systems such as the SPCZ and the western Pacific monsoon trough.

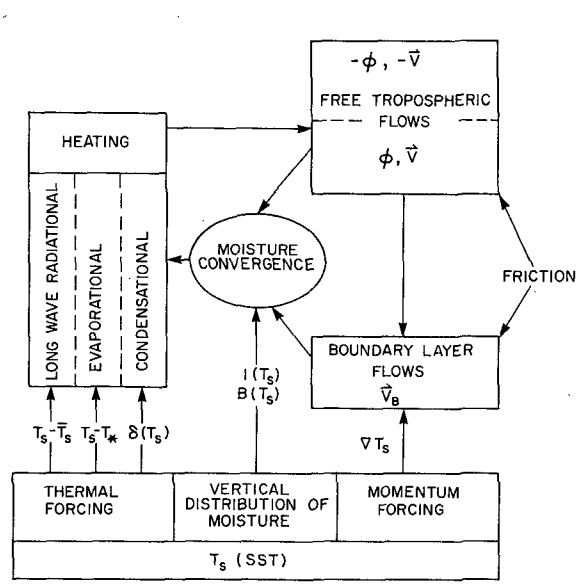

The direction and strength of the trade winds in both hemispheres and associated subtropical highs, near-equatorial trough, and southwest Pacific low pressure are also simulated reasonably well, rendering further investigation of both annual and interannual variations.

The model's thermodynamics has also been improved by implementing conventional CISK parameterization, based on the proposition that the degree or potential of convective instability of the tropical atmosphere increases with SST in a statistical sense, so that the occurrence and the rate of convective heating depend upon SST explicitly. This is consistent with the observed relationship between SST and HRC by Waliser and Graham (1991). Seager's (1991) and Kleeman's (1991) parameterization schemes are essentially equivalent; both are analogous to a CISK with reference to a threshold SST. The present SST-dependent CISK scheme yields an improved precipitation pattern.

Effects of a number of physical processes or factors on the tropical circulation are investigated. Inclusion of land–ocean thermal contrast by using an idealized land surface temperature that resembles an observed field has profound effects on the circulations nearby. The changes in land surface temperature, however, do not exhibit significant influences on remote oceanic regions. The ITCZ and SPCZ primarily owe their origin to the horizontal inhomogeneity of SST distribution. The South and North American continents contribute to their formation not through direct thermal effects but through indirect boundary effects that support upwelling changing the SST distribution. The diagnosis of observed climatological data indicates that nonlinear advection of momentum in the planetary boundary layer is of second-order importance. The momentum balance is approximately reached between pressure gradient and frictional forces in the equatorial oceanic waveguide (between 3°N and 3°S) and among the Coriolis, pressure gradient, and frictional forces outside the waveguide. The large meridional SST gradient in the subtropics is shown to have substantial influences on the strength and sense of the rotational trade winds and cross-isobaric winds.

The most salient discrepancy between the present model simulation and observations lies in the strength of the southeast trade winds in the southeast Pacific. The surface differential buoyancy fluxes associated with the SST gradient act as an important driving force in this region because of the remoteness of heating in the SPCZ and ITCZ. As pointed out in section 3, the boundary-layer momentum forcing associated with SST gradient increases with increasing depth of the boundary layer. A realistic simulation of the southeast trade needs a deeper boundary layer (2 km). What processes can actually account for the required stronger forcing in this region is unclear.

Within the model framework, many of the processes can be more realistically parameterized or described. For instance, the evaporation rate may rely on variable surface winds; the Newtonian cooling coefficient may vary with the amount of precipitation; the water vapor density scale height and static stability may depend upon SST; the boundary-layer depth may vary with SST and low-level divergence (to mimic the variation of the inversion height); and the boundary-layer friction coefficient may be a function of latitude and surface wind direction. We believe that both the model's dynamics and thermodynamics need to and can be further improved without invoking more vertical modes. The model's performance on simulating seasonal cycle and ENSO variabilities will be assessed and discussed elsewhere.

Acknowledgments. This research has been supported by a grant from the Climate Dynamics Division of the National Science Foundation (ATM 9019315) and by Tropical Ocean–Global Atmosphere program of NOAA under Grant NA90RAH00074 through the Joint Institute for Marine and Atmospheric Research. The authors thank Dr. Roger Lukas and anonymous reviewers for their comments. A large portion of the numerical computations was performed on the CRAY-YMP computer operated by the San Diego Supercomputer Center.

REFERENCES

Battisti, D. S., A. C. Hirst, E. S. Sarachik, and P. Tian, 1991: A consistent moist model for the relationship between anomalous surface winds and SST during ENSO events. *J. Atmos. Sci.*, submitted.

Betts, A. K., 1982: Saturation point analysis of moist convective overturning. *J. Atmos. Sci.*, **39**, 1484–1505.

Bjerknes, J., 1969: Atmospheric teleconnections from the equatorial Pacific. *Mon. Wea. Rev.*, **97**, 163–172.

Charney, J. G., and A. Eliassen, 1964: On the growth of the hurricane depression. *J. Atmos. Sci.*, **21**, 68–75.

Davey, M. K., and A. E. Gill, 1987: Experiments on tropical circulation with a simple moist model. *Quart. J. Roy. Meteor. Soc.*, **113**, 1237–1269.

Emmanuel, K. A., 1986: An air–sea interaction theory for tropical cyclones. Part I. *J. Atmos. Sci.*, **43**, 585–604.

Garcia, O., 1985: *Atlas of Highly Reflective Clouds for the Global Tropics:* 1971–1973. U.S. Department of Commerce, NOAA, Environmental Research Laboratory, Boulder, CO.

Gill, A. E., 1980: Some simple solutions for heat-induced tropical circulation. *Quart. J. Roy. Meteor. Soc.*, **106**, 447–462.

——, 1982: Studies of moist effects in simple atmospheric models: the stable case. *J. Geophys. Astrophys. Fluid Dyn.*, **19**, 119–152.

Graham, N., and T. P. Barnett, 1987: Observations of sea surface temperature and convection over tropical oceans. *Science*, **238**, 657–659.

Hoskins, B. J., 1983: Modeling of transient eddies and their feedback on the mean flow. *Large Scale Dynamical Processes in the Atmosphere*, B. J. Hoskins and R. P. Pearce, Eds., Academic Press, 397 pp.

——, and P. D. Sardeshmukh, 1987: Transient eddies and seasonal mean rotational flow. *J. Atmos. Sci.*, **44**, 328–338.

Kiladis, G. N., H. v. Storch, and H. van Loon, 1989: Origin of the South Pacific convergence zone. *J. Climate*, **2**, 1185–1195.

Kleeman, R., 1991: A simple model of atmospheric response to ENSO sea surface temperature anomalies. *J. Atmos. Sci.*, **48**, 3–18.

Kuo, H.-L., 1974: Further studies of the parameterization of the influence of cumulus convection on large-scale flow. *J. Atmos. Sci.*, **31**, 1231–1240.

Lindzen, R. S., and S. Nigam, 1987: On the role of sea surface temperature gradients in forcing low-level winds and convergence in the tropics. *J. Atmos. Sci.*, **45**, 2440–2458.

Madden, R. A., and P. R. Julian, 1972: Description of global-scale circulation cells in the tropics with a 40–50 day period. *J. Atmos. Sci.*, **29**, 1109–1123.

Matsuno, T., 1966: Quasi-geostrophic motions in the equatorial area. *J. Meteor. Soc. Japan, Ser. II*, **44**, 25–43.

Neelin, J. D., 1988: A simple model for surface stress and low-level flow in the tropical atmosphere driven by prescribed heating. *Quart. J. Roy. Meteor. Soc.*, **114**, 747–770.

——, 1989: On the interpretation of the Gill model. *J. Atmos. Sci.*, **46**, 2466–2468.

——, and I. M. Held, 1987: Modeling tropical convergence based on the moist static energy budget. *Mon. Wea. Rev.*, **115**, 3–12.

Ooyama, K., 1964: A dynamic model for the study of tropical cyclone development. *Geofis. Int.* (Mexico), **4**, 187–198.

Philander, G. J. H., T. Yamagata, and R. C. Pacanowski, 1984: Unstable air–sea interactions in the tropics. *J. Atmos. Sci.*, **41**, 604–613.

Riehl, H., 1979: *Climate and Weather in the Tropics.* Academic Press, 611 pp.

Rui, H., and B. Wang, 1990: Development characteristics and dynamic structure of tropical intraseasonal convection anomalies. *J. Atmos. Sci.*, **47**, 357–379.

Sadler, J. C., M. A. Lander, A. M. Hori, and L. K. Oda, 1987: Tropical marine climatic atlas. Vol. 2, Pacific Ocean. Report UHMET 87-02, Department of Meteorology, University of Hawaii, Honolulu, Hawaii, 27 pp.

Seager, R., 1991: A simple model of climatology and variability of the low-level wind field in the tropics. *J. Climate*, **4**, 164–179.

Tomasi, C., 1984: Vertical distribution features of atmospheric vapor in the Mediterranean, Red Sea, and Indian Ocean. *J. Geophys. Res.*, **89**(D2), 2563–2566.

Waliser, D. E., and N. E. Graham, 1993: A comparison of the highly reflective cloud and outgoing longwave radiation data sets. *J. of Climate*, **6**, submitted

Wang, B., 1988: The dynamics of tropical low frequency waves: An analysis of moist Kelvin waves. *J. Atmos. Sci.*, **45**, 2051–2065.

——, 1992: The vertical structure and development of the ENSO anomaly mode during 1979–1989. *J. Atmos. Sci.*, **49**, 698–712.

——, and J.-K. Chen, 1989: On the zonal-scale selection and vertical structure of equatorial intraseasonal waves. *Quart. J. Roy. Meteor. Soc.*, **115**, 1301–1323.

——, and H. Rui, 1990: The dynamics of coupled moist Kelvin–Rossby waves on an equatorial beta-plane. *J. Atmos. Sci.*, **47**, 397–413.

Weare, B. C., 1986: A simple model of tropical atmosphere driven by a circulation-dependent heating. *Quart. J. Roy. Meteor. Soc.*, **112**, 409–429.

Webster, P. J., 1981: Mechanisms determining the atmospheric response to sea surface temperature anomalies. *J. Atmos. Sci.*, **38**, 554–571.

Yanai, M., S. Esbensen, and J.-H. Chu, 1973: Determination of bulk properties of tropical cloud clusters from large-scale neat and moisture budgets. *J. Atmos. Sci.*, **30**, 611–627.

Young, J. A., 1987: Boundary layer dynamics of tropical and monsoonal flows. *Monsoon Meteorology*, C.-P. Chang and T. N. Krishnarmurti, Eds., Oxford, 461–500.

Zebiak, S. E., 1982: A simple atmosphere model of relevance to El Niño. *J. Atmos. Sci.*, **39**, 2017–2027.

——, 1986: Atmospheric convergence feedback in a simple model for El Niño. *Mon. Wea. Rev.*, **114**, 1263–1271.

——, and M. A. Cane, 1987: A model El Niño–Southern Oscillation. *Mon. Wea. Rev.*, **115**, 2262–2278.